The 21 May 1960 M_w 8.1 Concepción Earthquake: A Deep Megathrust Foreshock That Started the 1960 Central-South Chilean Seismic Sequence

Javier Ojeda[*1], Sergio Ruiz[1], Francisco del Campo[2], and Matías Carvajal[3,4]

Abstract

One of the most notable seismic sequences in modern times was recorded in May 1960 along the southern Chilean subduction zone. The sequence started on 21 May with the M_w 8.1 Concepción earthquake; 33 hr later the M_w 9.5 Valdivia megathrust earthquake occurred, the largest ever recorded in the instrumental period. These events changed the geomorphology of the coast along more than 1000 km, generated extensive structural damage in the main cities of central-south Chile, and triggered a Trans-Pacific tsunami. Observed land-level changes due to both earthquakes were reported in 1970. These observations were ascribed to both events but have been used to study only the general source properties of the 22 May Valdivia mainshock. Here, we separate these data to constrain for the first time the slip distribution of the 21 May Concepción earthquake, applying a Bayesian approach that considers uncertainties in the data. Our results show that the M_w 8.1 Concepción earthquake ruptured a deep segment of the megathrust, concentrated in a compact zone below the Arauco peninsula between depths of 20 and 50 km. Tsunami generation from this deep source agrees well with the tsunami arrival times and small amplitudes recorded by tide gauges along the Chilean coast. Our study highlights the importance of the 21 May 1960 Concepción earthquake in the context of large historical Chilean earthquakes.

Cite this article as Ojeda, J., S. Ruiz, F. del Campo, and M. Carvajal (2020). The 21 May 1960 M_w 8.1 Concepción Earthquake: A Deep Megathrust Foreshock That Started the 1960 Central-South Chilean Seismic Sequence, *Seismol. Res. Lett.* **XX**, 1–11, doi: 10.1785/0220190143.

Supplemental Material

Introduction

The May 1960 central-south Chile earthquakes arguably represent the most important seismic sequence that has occurred in modern times. The sequence took place in the southern portion of the subduction zone formed between the Nazca and South America plates that converge at 6–7 cm/yr (Altamimi *et al.*, 2007). The sequence started with the M_w 8.1 Concepción event at 10:02:52 UTC on 21 May 1960. No foreshocks were observed in teleseismic data (Cifuentes, 1989). Several aftershocks were reported in the International Seismological Centre (ISC) catalog and relocated by Cifuentes (1989), all of which took place in a limited zone below the Arauco peninsula (Fig. 1). Thirty-three hours later, a long-period nucleation phase of large-scale slip began, presumably between the downgoing oceanic lithosphere and weaker asthenosphere, which likely triggered the M_w 9.5 Valdivia mainshock 15 min later (Kanamori and Cipar, 1974; Cifuentes and Silver, 1989; Linde and Silver, 1989).

The 1960 earthquakes produced extensive surface deformation along 1000 km of the coast, from the Arauco peninsula in the north (~37° S) to the Taitao peninsula near the Chile triple junction in the south (~46° S). Such regional-scale deformation was quantified in 1968 by George Plafker from the U.S. Geological Survey (Fuis *et al.*, 2015) and was reported two years later in the work of Plafker and Savage (1970; hereafter, PS70). Uplift observations reached 5.7 m offshore the continent and decreased landward down to 2.7 m of subsidence. The PS70 report also includes deformation data further inland obtained from pre- and postgeodetic surveys by the Military Geographic Institute (IGM) of Chile.

The land-level changes reported in PS70 have been the main dataset used to estimate the slip distribution of the 22 May 1960 Valdivia mainshock. The first interpretation of these data was made by PS70 and Plafker (1972), who proposed a simple source model with over 20 m of uniform slip on a fault plane approximately 1000 km long and 60 km wide. A few decades

1. Departamento de Geofísica, Universidad de Chile, Santiago, Chile; 2. Centro Sismológico Nacional, Universidad de Chile, Santiago, Chile; 3. Escuela de Ciencias del Mar, Pontificia Universidad Católica de Valparaíso, Valparaíso, Chile; 4. Millennium Nucleus The Seismic Cycle along Subduction Zones, Valdivia, Chile

*Corresponding author: jojeda@dgf.uchile.cl

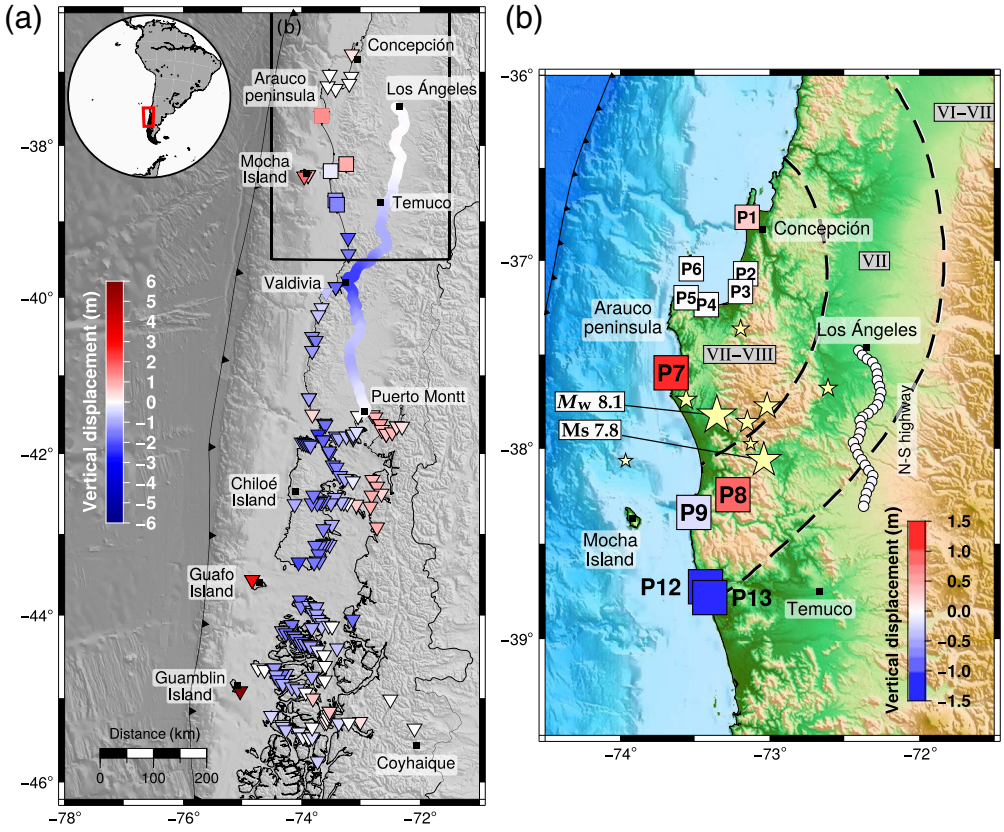

Figure 1. Vertical displacement changes due to the May 1960 earthquakes compiled by Plafker and Savage (1970; hereafter, PS70). (a) Uplift and subsidence associated with the M_w 9.5 Valdivia earthquake (inverted triangles) and M_w 8.1 Concepción earthquake (squares) along with an inset map showing the study location with reference to South America. The continous line inland corresponds to vertical changes along the north–south highway. (b) Data associated with the M_w 8.1 Concepción earthquake. Large squares are the data described by PS70, small squares correspond to vertical changes near the zone of the Concepción earthquake, and the continuous line inland corresponds to the segment of the north–south highway. Dashed lines are the Medvedev–Sponheuer–Karnik (MSK) macroseismic intensities reported by Astroza and Lazo (2010), which separate the structural damage due to the 21 May earthquake. Stars are the events with **M** > 5.8 that occurred after the M_w 8.1 Concepción earthquake and before the Valdivia megathrust earthquake. The color version of this figure is available only in the electronic edition.

later, Barrientos and Ward (1990) inverted the data to obtain a heterogeneous slip distribution, which was later improved by Moreno *et al.* (2009), who considered more realistic surface fault properties. The data were more recently combined with both near- and far-field tsunami records to further improve these results (Fujii and Satake, 2013; Ho *et al.*, 2019). These different works coincide with the main aspects of the slip distribution of the 1960 earthquakes, reporting an ~900 km long rupture and magnitudes on the order of M_w 9.2–9.4, smaller than the M_w 9.5–9.6 range estimated from low-frequency waves (Kanamori and Anderson, 1975; Cifuentes and Silver, 1989). However, all of these studies ignored the effects on land-level changes caused by the large foreshock of 21 May, despite the clear distinction of the data made in PS70. Addressing the source properties of this "forgotten earthquake" has important seismotectonic implications for the region that has experienced giant historical earthquakes (Cisternas *et al.*, 2005; Cisternas, Carvajal, *et al.*, 2017; Cisternas, Garrett, *et al.*, 2017; Ruiz and Madariaga, 2018) and may provide clues about the beginning phase of the largest earthquake ever recorded in human history.

In this work, we reinterpret the PS70 data to separate the coastal vertical displacements due to the 21 May 1960 Concepción earthquake and provide for the first time a slip distribution for this event. To this end, we use a Bayesian inversion approach that considers the unavoidable uncertainties in the reported data. Our slip distribution is further verified by comparing predicted tsunami arrival times, amplitudes, and wave periods with those recorded by tide gauges along the Chilean coast, which have not been analyzed to date.

The 21 May 1960 Earthquake

Cifuentes and Silver (1989) proposed a seismic moment of 2×10^{21} N · m for Concepción earthquake using the Tsukuba (TSK) record from the Earthquake Research Institute in Japan, which they mention has sufficiently good quality. Cifuentes (1989) discussed how this seismic moment is consistent with the 150 km long segment where coastal level changes associated to this event were reported by PS70. This rupture zone correlates well with the isoseismal map made by Astroza and Lazo (2010) based on Medvedev–Sponheuer–Karnik (MSK) macroseismic intensities inferred in central-south Chilean cities from engineering reports, local newspapers, and magazines of the time (Fig. 1b). According to Astroza and Lazo (2010), damage from the Concepción earthquake could be easily distinguished from that associated with the Valdivia mainshock and was concentrated along 300 km between 35.5° S and 39° S, whereas severe damage was confined to the Arauco peninsula within a 150 km long area (VII–VIII region of Fig. 1b). Several aftershocks followed the 21 May earthquake, including eight earthquakes **M** > 5.8 reported by Cifuentes (1989) (see Fig. 1b). The largest one had

TABLE 1
Comparisons among Models for the 21 May 1960 M_w 8.1 Concepción Earthquake

Parameter	Model A	Model B	Model C	Model D
Dataset	A: P7, P8, P9, P12, P13	B: P7, P8, P9, P12	C: P7, P8, P9	D: P7, P8, P9, P1, P3, P4, P5, north–south highway
Seismic moment M_0 (N · m)	1.86×10^{21}	1.62×10^{21}	1.46×10^{21}	1.98×10^{21}
Magnitude M_w	8.11	8.07	8.04	8.13
Centroid depth (km)	29	31	35	39
Maximum slip (m)	3.58	3.44	3.44	3.03
Mean slip (m)	0.59	0.52	0.54	0.54
Rms (m)	0.78	0.67	0.43	0.15

Rms, root mean square.

a magnitude of M_s 7.8 and occurred 15 min before the 22 May Valdivia earthquake (Kanamori and Cipar, 1974; Cifuentes, 1989). Similar to the 1960 M_w 9.5 Valdivia earthquake, the 21 May earthquake also triggered a tsunami (Berninghausen, 1962; Sievers *et al.*, 1963); however, the amplitudes were much smaller (see Fig. S1). At least six tide gauge stations deployed along the Chilean coast recorded relatively small tsunami following the Concepción earthquake and before the arrival of the large tsunami waves of the Valdivia mainshock (Fig. S1).

Vertical Displacements Data

We use geological and geodetic data compiled by PS70, who quantified the vertical changes associated with the 1960 earthquakes along the coast and in some islands in central-south Chile. In addition to reporting shoreline changes in 155 localities, they considered vertical tectonic displacements inland published in geodetic surveys by the IGM of Chile (Fig. 1a). The data in PS70 may be affected by approximately eight years of postseismic deformation and may also include preseismic effects. Nonetheless, PS70 reported small postseismic vertical displacements by analyzing 20 measures obtained shortly after the 1960 earthquakes (Saint-Amand, 1961; Alvarez, 1963; Galli and Sanchez, 1963; Thomas *et al.*, 1963; Weischet, 1963; and others).

Vertical displacements were determined with various methods: differences between pre- and postearthquake growth of terrestrial vegetation, changes in the positions of tide lines reported by local residents, upper growth limits of mussels and estimates by port authorities and local residents (Fig. 1a). Observations were mainly made at bedrock sites; nevertheless, in 12 sites, they were made on unconsolidated deposits where some nontectonic superficial subsidence may have occurred. To each vertical report they assigned an error of 0.2, 0.4, or 0.6 m for good, fair, and poor estimates, respectively. PS70 designated a nonquantified error for the sites reported by local residents (e.g., sites P2 and P6); in this study, we do not consider the measurements on these sites. Vertical tectonic changes inland were measured along the north–south highway from Los Ángeles to Puerto Montt cities (Fig. 1a). The IGM gathered information through the pre-earthquake leveling survey of 1957–1959 and the post-earthquake leveling survey of 1963–1964. This information was digitized at 150 sites along a leveling line, and we assigned an error of 0.13 m for each measure, according to the uncertainties fixed by Barrientos and Ward (1990).

According to PS70, most of these vertical displacements correspond to the deformation associated with the 22 May Valdivia earthquake. However, based on eyewitnesses reports, PS70 were able to distinguish surface displacements caused by the 21 May Concepción earthquake (Fig. 1b; see the Time sequence of the movements section in PS70 for more details, 1016 pp.). In particular, they identified and reported the land-level changes that took place south of the Arauco peninsula at the time of the Concepción foreshock. Furthermore, based on interviews with port authorities and local residents, they concluded that Mocha Island did not experience vertical displacements due to the earthquake of 21 May. In summary, PS70 delimited five sites corresponding to the surface deformation of the 21 May event.

In this work, we assess the slip distribution of the 21 May 1960 Concepción earthquake using four different datasets of vertical displacements associated to the event. Following the assumptions and interpretations of PS70, we consider the whole amount of vertical changes listed for the 21 May earthquake. The datasets were built based on the quality of the data and considering some sites near to the main rupture area, specifically along the Arauco peninsula and a segment of the line-leveling inland that could experience vertical displacement due to the Concepción event (Fig. 1b, see Table S1). The different datasets used in this study are shown in Table 1.

Method

We estimate the slip distribution of the 21 May earthquake from the vertical displacement data using an inversion technique. To

model the elastic deformation due to an interplate event, we make the following assumptions and simplifications. The plate contact is approximated by the Nazca plate upper surface model published by Tassara and Echaurren (2012), which we discretized in n cells of approximately 10 km × 10 km (n ranges from 750 to 930, depending on the dataset used). The lithosphere is assumed to be a linearly elastic, homogeneous, and isotropic half-space (see Fig. S2). Slip at the ith subfault is decomposed into the along-strike and up-dip components of slip $u_i^{(1)}$ and $u_i^{(2)}$. These parameters can be arranged in a vector $\mathbf{m} = (u_1^{(1)}, \ldots, u_n^{(1)}, u_1^{(2)}, \ldots, u_n^{(2)})$. We only have vertical displacement data, which we arrange in the vector $\mathbf{d}$. The forward model can be written as $\mathbf{d}^{\text{pred}} = \mathbf{Gm}$, in which $\mathbf{G}$ is the kernel matrix.

We solve the inverse problem following a Bayesian approach, which describes states of information about the model and the data through probability density functions (PDFs). The idea is to combine information sources (observations, *a priori* knowledge, and the forward model) to recover an *a posteriori* information state. Using the notation and formalism of Tarantola (2005), the *a posteriori* PDF of the model $\sigma_M(\mathbf{m})$ is given by

$$\sigma_M(\mathbf{m}) = \eta \rho_M(\mathbf{m}) \rho_D(\mathbf{Gm}), \tag{1}$$

in which $\rho_M(\mathbf{m})$ and $\rho_D(\mathbf{d})$ are PDFs containing the *a priori* information of the model and data, respectively. η is a normalization constant that ensures that $\sigma_M(\mathbf{m})$ integrates 1 over the whole space.

We assume that $\rho_D(\mathbf{d})$ represents a normal distribution with mean $\mathbf{d}_{\text{obs}}$ (observed data) and covariance matrix $\mathbf{C}^{(d)}$, which contains the instrumental uncertainties. Similarly, $\rho_M(\mathbf{m})$ represents a normal distribution with mean $\mathbf{0}$ and covariance matrix $\mathbf{C}^{(m)}$. By definition, $\mathbf{C}^{(m)}$ quantifies the spatial autocorrelation of the slip field, that is, the correlations between the values of the slip at pairs of points. Similar to Radiguet *et al.* (2011), we assume that the covariance decays exponentially with the distance between the subfaults and that the slip field is isotropic. The exponential function, in contrast to a Gaussian, allows to stabilize the solution at large distances Radiguet *et al.* (2011). Thus, the covariance matrix of the model parameters takes the following form.

$$\mathbf{C}^{(m)} = \left[\begin{array}{c|c} \mathbf{B} & \mathbf{0} \\ \hline \mathbf{0} & \mathbf{B} \end{array}\right], \tag{2}$$

with $\mathbf{B}$ given by

$$B_{ij} = \left(\sigma^{(u)} \frac{\lambda^{(0)}}{\lambda}\right)^2 \exp\left(-\frac{d(i,j)}{\lambda}\right), \tag{3}$$

in which λ is the correlation length and controls the distance over which the slip is self-correlated (we used $\lambda = 25$ km for each model), $\lambda^{(0)}$ is a scaling factor fixed to 10 km (about the size of a subfault), $\sigma^{(u)}$ is the *a priori* standard deviation of the slip (controls the damping effect), and $d(i,j)$ is the distance between the ith and jth subfaults.

With these considerations, we have

$$\sigma_M(\mathbf{m}) = \kappa(\mathbf{d}_{\text{obs}}) \exp(-\varphi(\mathbf{m}; \mathbf{d}_{\text{obs}})), \tag{4}$$

$$\varphi(\mathbf{m}; \mathbf{d}_{\text{obs}}) = \frac{1}{2}\{(\mathbf{Gm} - \mathbf{d}_{\text{obs}})^t \mathbf{C}^{(d)^{-1}} (\mathbf{Gm} - \mathbf{d}_{\text{obs}}) + \mathbf{m}^t \mathbf{C}^{(m)^{-1}} \mathbf{m}\}. \tag{5}$$

Rearranging the terms in equation (5), we conclude that the *a posteriori* state of information is described by a normal distribution with mean $\hat{\mathbf{m}}$ and covariance matrix $\hat{\mathbf{C}}^{(m)}$ defined by

$$\hat{\mathbf{m}} = \hat{\mathbf{C}}^{(m)} \mathbf{G}^t \mathbf{C}^{(d)^{-1}} \mathbf{d}_{\text{obs}}, \tag{6}$$

$$\hat{\mathbf{C}}^{(m)} = \{\mathbf{C}^{(m)^{-1}} + \mathbf{G}^t \mathbf{C}^{(d)^{-1}} \mathbf{G}\}^{-1}. \tag{7}$$

More explicitly,

$$\sigma_M(\mathbf{m}) = \eta' \exp\left(-\frac{1}{2}(\mathbf{m} - \hat{\mathbf{m}})^t \hat{\mathbf{C}}^{(m)^{-1}} (\mathbf{m} - \hat{\mathbf{m}})\right). \tag{8}$$

We add additional *a priori* information by imposing that at each subfault the rake has a valid range around the direction of plate convergence. It can be shown that this is equivalent to $\mathbf{Qm} \geq \mathbf{0}$, with $\mathbf{Q}$ a matrix that projects the slip vector in two directions. This condition is expressed by the following PDF:

$$R(\mathbf{m}) = \begin{cases} 1 & \text{if } \mathbf{Qm} \geq \mathbf{0} \\ 0 & \text{otherwise} \end{cases}. \tag{9}$$

To update our knowledge we merge $R(\mathbf{m})$ into $\sigma_M(\mathbf{m})$ by multiplying both PDFs, as we did in equation (1).

$$\tilde{\sigma}_M(\mathbf{m}) = \tilde{\eta} R(\mathbf{m}) \exp\left(-\frac{1}{2}(\mathbf{m} - \hat{\mathbf{m}})^t \hat{\mathbf{C}}^{(m)^{-1}} (\mathbf{m} - \hat{\mathbf{m}})\right). \tag{10}$$

Our restricted solution is the maximum likelihood model, that is, the maximum of the function $\tilde{\sigma}_M(\mathbf{m})$. This approach has been used in other studies to estimate the slip distribution patterns of different earthquakes (Ruiz *et al.*, 2016, 2017).

Slip Distribution of the Concepción Earthquake

For each vertical displacement datasets considered (Table 1), we estimate slip distributions performing a Bayesian inversion to include the uncertainties in the PS70 data. The resulting slip models (Fig. 2) show similar along-dip features characterized by an ~150 km long rupture confined to the deep portion of

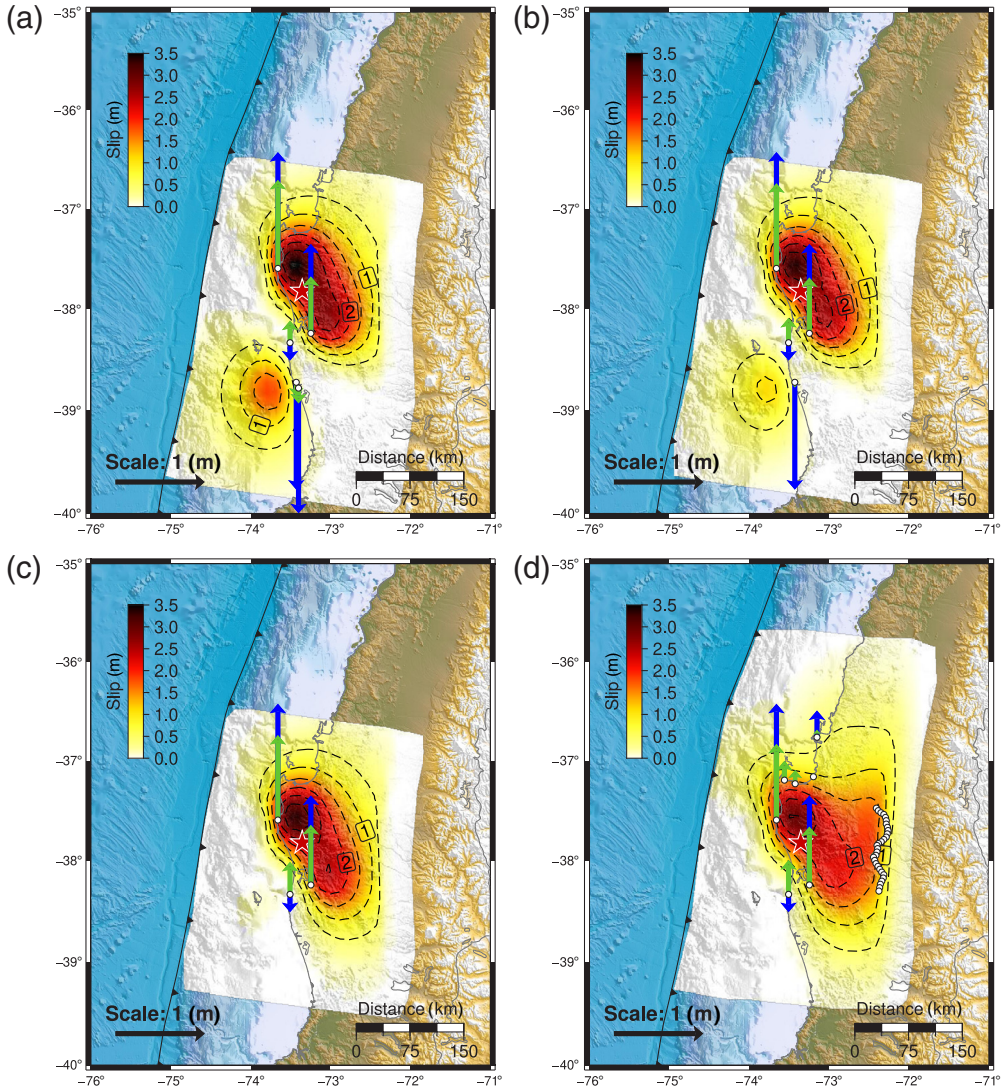

Figure 2. Slip distribution of the M_w 8.1 Concepción earthquake that occurred on 21 May 1960. The isoslip segmented lines are shown each 0.5 m. The white dots represent the sites used in each model. Blue vectors represent observations, and green represents the simulated data. (a) Model A, considering five sites. (b) Model B, considering four sites. (c) Model C, considering three sites. (d) Model D, considering seven sites and the north–south highway segment (30 sites). The datasets for each model are summarized in Table 1. The color version of this figure is available only in the electronic edition.

the plate interface, approximately between depths of 20 and 50 km below sea level, with a moment magnitude M_w 8.0–8.1 and a maximum slip between 3–3.6 m. However, some differences are obtained using the four datasets, which are described subsequently.

Model A

The slip distribution model obtained considering the five sites that PS70 recognized as tectonic movements produced by the 21 May earthquake (dataset A) is shown in Figure 2a (model A). In this case, the main rupture occurred in the deeper area of the plate interface below the Arauco peninsula. However, model A shows an additional slip patch to the south of the main rupture zone. This offshore patch is controlled by two subsidence measurements, sites P12 and P13, which have poor quality. Furthermore, because site P12 is located on unconsolidated deposits, it may have experienced nontectonic deformation, and therefore, the measurement may not be correct. The centroid of model A is located at a depth of 29 km, and the maximum slip is 3.58 m. Considering a shear modulus of 40 GPa, we obtain a seismic moment of 1.86×10^{21} N · m, which is equivalent to a magnitude M_w 8.11.

Model B

Discarding the measurement over site P13, which have poor quality (dataset B), we obtain the slip distribution shown in Figure 2b (model B). The slip distribution of model B preserves the main features of model A, but the offshore patch located below Mocha Island partially disappears. We obtain a seismic moment of 1.62×10^{21} N · m and a moment magnitude M_w 8.07.

Model C

Because of the impact of large subsidences measurements of up to 1 m at the site P12, and considering that is localized over unconsolidated soil deposits, we estimate the slip distribution with three measurements (dataset C) of good quality and the one with fair quality showing a minor subsidence (Fig. 2c, model C). This model agrees with the distribution and location of slip from the other two models but shows a large difference in the slip below Mocha Island, which according to local interviews was not vertically displaced. In this case, the centroid is located at 35 km depth, and the maximum slip is 3.44 m. The seismic moment for model C is 1.46×10^{21} N · m, equivalent to a moment magnitude M_w 8.04.

Model D

To explore the influence that the inland data obtained along the north–south highway has on the slip distribution, we

estimate a fourth slip model, named model D. This model considers the three sites of model C but also the nearby sites on the Arauco peninsula, specifically some measurements in the north and along the leveling line from Los Ángeles to northern Temuco (dataset D). This slip distribution model (Fig. 2d, model D) maintains features similar to those of the other models with the main rupture confined below the Arauco peninsula but with a northeastward extension to the deeper zone of the plate interface with up to 1 m of slip. This northeastward extension is required to match the vertical displacements along the leveling line measured by the IGM (see Fig. S3). As in the other models, in model D, we obtain a moment magnitude M_w 8.13 and a slightly smaller maximum slip of 3 m.

General slip parameters

In Table 1, we present the main slip parameters of each model together with their respective root mean square (rms) errors from

$$\mathrm{rms} = \sqrt{\frac{1}{N}\sum_{i=1}^{N}(du_i^{\mathrm{pred}})^2}, \tag{11}$$

in which du^{pred} corresponds to the predicted displacements, du_i are the observed displacements, and N is the number of sites considered. Model D has a smaller rms than other models, which is explained by the larger number of observations (37 sites) and the good fit of vertical displacements along the north–south highway (Fig. S3). Nevertheless, in this case it remains unclear to what extent the data along the leveling line is influenced by the 22 May mainshock.

The spatial resolutions of our slip distributions are verified by checkerboard tests with patches of 60 km × 60 km (see Fig. S4). The test indicates good resolutions in the area where most slip was resolved, which gradually decays seaward toward the trench, according to the spatial distribution of vertical displacements on the surface. Checkerboard tests for models A, B, and D shown in Figure S4a,b,d, respectively, can reproduce the synthetic displacements well; nonetheless, this performance is attributed to the use of larger datasets with a better coverage, and not necessarily to a well solved inversion of slip distributions of the Concepción earthquake. Instead, the checkerboard test for model C (Fig. S4c) is poorly constrained because only three observation sites were employed.

In summary, models A and B maintain similar slip distribution features with a high rms and a well-solved checkerboard test. However, the slip patch up to 1 m in the south of Mocha Island is not consistent with the assumptions of PS70. Model C reproduces the observations well with lower rms, considering the uncertainties that can be at least 15% of the vertical displacement for the dataset analyzed, but the checkerboard test is not well solved due the low number of sites used. Despite this, model C presents a simple main asperity at the bottom of the plate interface with a peak slip of ~3.4 m. Model D has the smallest rms and the better checkerboard test, but the use of north–south highway vertical displacement could be incorrect by the possible influence of the mainshock event. Given the few observations sites employed, we test the performance of the slip distribution models with additional observations from tsunami records for the 21 May Concepción earthquake.

Sensitivity test

Our models have similar features because they are strongly affected by correlation length (λ) and damping (σ). We assess the influence of λ and σ parameters in the inversion using the sites P7, P8, and P9 and additional sites P1, P3, P4, and P5 (see Fig. S5). The results have shown that a lower σ underestimates the slip amount and does not reproduce well the observations, independent of the λ used. However, greater values of σ can reproduce well the surface observations, with lower rms, but yield complex slip distributions with remarkable slip amount below Mocha Island, that likely did not experience significant vertical displacement. The parameters obtained in the sensitivity test are summarized in Table S2.

Slip Models Performance Judged by Tsunami Observations

Tsunami records and modeling

We test the performance of the obtained slip distribution models against tsunami records of the 21 May Concepción earthquake. Tsunami signals of this event were identified and extracted from the mareograms originally published for the 22 May Valdivia tsunami in Barros and Sievers (1961). Likely because of the small tsunami amplitudes relative to those of the mainshock, the tsunami signals of the 21 May Concepción earthquake were overlooked and therefore have not been analyzed to date. At least six tide gauge stations recorded the 21 May tsunami along the Chilean coast in Arica, Antofagasta, Caldera, Coquimbo, Valparaíso, and Talcahuano (see Fig. S1), all located to the north of the 21 May earthquake source. To estimate the amplitudes, periods, and arrival times of the 21 May tsunami we: (1) digitized the mareograms, (2) estimated the dominant tidal components through a harmonic least-squares fit, and (3) removed these components from the original records (Fig. S1). We could not accurately digitize the Caldera record because of its very low signal-to-noise ratio, likely caused by specific local topobathymetric conditions where the station was located (Barros and Sievers, 1961).

The extracted and processed tsunami records are compared with tsunami predictions from each of the obtained slip distribution models. This process constitutes a key test to verify our results, because tsunami observations were not used in the slip inversions. To this end, we use the Cornell Multi-grid Coupled Tsunami model (COMCOT) to compute tsunami waveforms at the five sites where tsunami records were obtained. This model solves the linear and nonlinear shallow water equations (LSWE

and NLSWE, respectively) using a leap-frog scheme on a staggered and nested grid system (Wang, 2009). We represent the bathymetry offshore Chile by a two-level nested grid system with increasing spatial resolution at sites where observations are available. For the first level grid of 30 arcsec spatial resolution, we use the General Bathymetric Chart of the Oceans bathymetry (GEBCO) and consider the LSWE. In coastal areas, we downsample the bathymetric data to 5 arcsec, consider the NLSWE, and assume the effects of bottom friction using a Manning's roughness coefficient of 0.025 $s\,m^{-1/3}$ (Kotani *et al.*, 1998). For the three sites closest to the source (i.e., Talcahuano, Valparaíso, and Coquimbo), we use local measurements from nautical charts to represent specific features of the seafloor that may affect shallow water propagation. In all cases, the initial conditions for tsunami propagation are the vertical deformation beneath the sea estimated for each slip model using the elastic half-space dislocation model of Okada (1985) (Fig. 3).

Tsunami triggered by the 21 May earthquake against model predictions

In general, all slip models predict tsunamis that reasonably match the tide gauge records deployed along the Chilean coast. In Figure 4, we show the resulting waveforms for model C (light blue) superimposed over the observed (black) tsunamis in Arica, Antofagasta, Coquimbo, Valparaíso, and Talcahuano. For Talcahuano, we also plot the waveform predicted by model D (red line), which is discussed subsequently. The results for the other three models are shown in Figure S6.

The amplitudes of the tsunamis triggered by the 21 May Concepción earthquake along the Chilean coast were small, reaching no more than 50 cm in Talcahuano but mainly less than 10 cm elsewhere. These values are significantly less than the local tide ranges of 1.5–2 m, which may explain why the 21 May tsunamis were not reported by eyewitnesses. It is not surprising to see that amplitudes do not necessarily decrease with distance from the source. For example, the amplitudes at the station in Arica, the farthest from the source, were larger than those at sites much closer to the source such as Valparaíso. Tsunami amplitudes depend not only on the distance from the source or on directivity effects but also on the local bathymetry near the stations, which may induce large local amplification processes (e.g., bay and/or shelf resonance) (Cortés *et al.*, 2017). Our low-quality bathymetric data in the tsunami-sensitive region of Arica may also explain why modeled tsunamis poorly predict the observed tsunami patterns of later wave phases.

Aside from the waveform predicted by model D in Talcahuano (red line in Fig. 4), the arrival times, leading wave amplitudes and polarities (i.e., initial sea level rise or drawdown) predicted at all stations are consistent with those recorded, especially at the three stations that are closest to the source and have better bathymetric data. For example, although a 22 cm positive leading wave was observed at Talcahuano 67 min after the mainshock (black line), model-predicted tsunamis indicate a similar

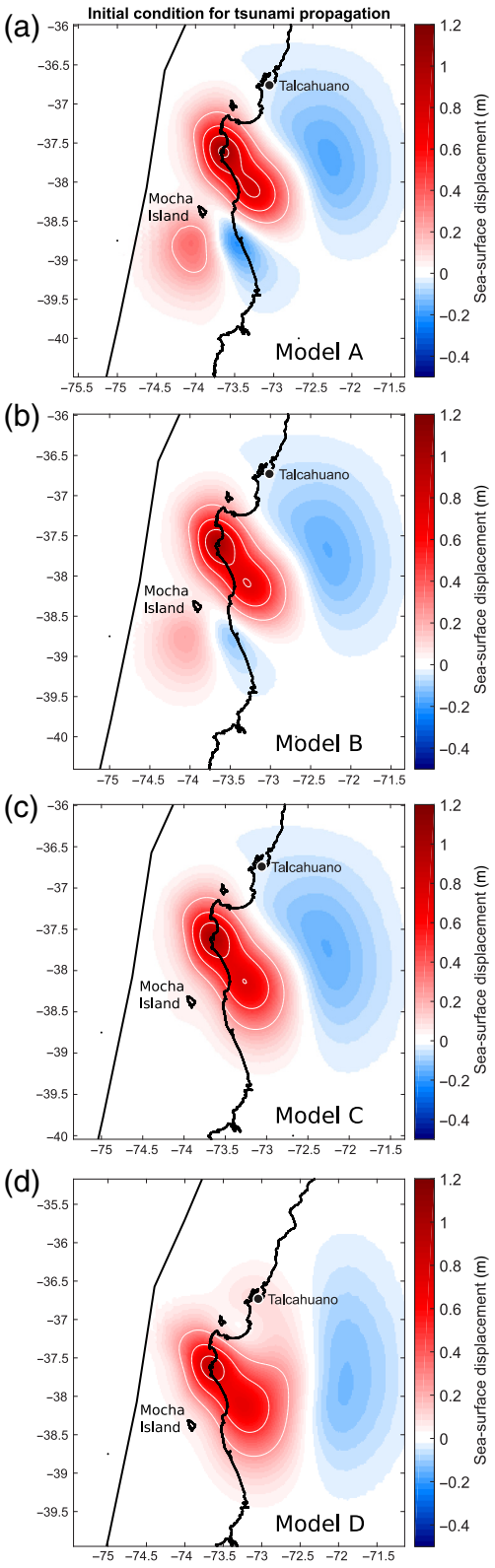

Figure 3. Coseismic vertical surface deformation patterns used as initial conditions for tsunami propagation in (a) model A, (b) model B, (c) model C, and (d) model D. Note the vertical displacement in Mocha island for the different models and the uplift near Talcahuano (site P1) that reproduce the Model D instead the subsidence estimated by models A, B, and C. The color version of this figure is available only in the electronic edition.

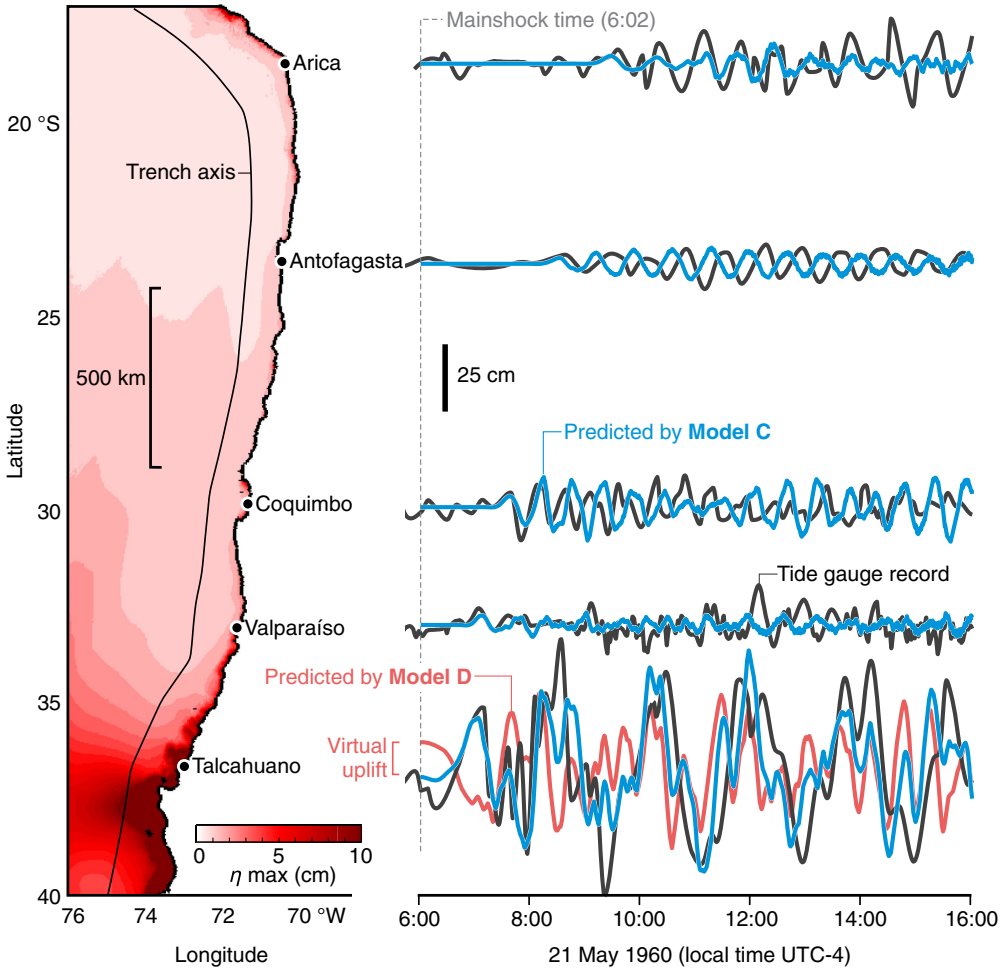

Figure 4. Comparison between modeled and observed tsunamis for the 21 May Concepción earthquake along the Chilean coast. The left panel shows the maximum sea surface elevation (η max) in centimeters predicted by model C during 10 hr of simulation and the sites where tsunamis were recorded by tide gauges. The right panel shows the observed tsunami waveforms (black) and those predicted by model C (light blue). The red waveform in Talcahuano is the predicted tsunami by model D. Note the virtual uplift of the synthetic mareogram produced by the vertical deformation predicted by model D. In a real situation, the movement of the tide gauge would be in the opposite sense, because uplift of the seafloor beneath the tide gauge would produce an instantaneous or gradual decrease in the water column. The resulting waveforms for the other models are shown in Figure S6. The color version of this figure is available only in the electronic edition.

positive leading wave with an amplitude of 20 cm arriving 62 min after the mainshock. This good fit, also seen at the other stations for all slip distribution models (Fig. S6), is notable considering the potential digitization errors of the old, low signal-to-noise mareograms and the uncertainties of the bathymetric data. Model D, however, fails to predict the observed tsunami waveform in Talcahuano (Fig. 4). This model would produce coseismic uplift in Talcahuano (Fig. 3d), consequently affecting the spatiotemporal features of the leading wave, which suggests that the northeast extension of the slip obtained there probably did not occur, even though its rms is the lowest among the models here considered.

In summary, our tsunami modeling test gives us confidence that the main features of our slip distributions are robust, except for that of model D, which fails to reasonably predict the tsunami waveform in the station closest to the source region. Because of this, our preferred slip distribution inversion correspond to model C (Fig. 2c), which is a simple main asperity at the bottom of the plate interface.

Discussion

A deep megathrust rupture for the 21 May Concepción earthquake

The four slip distribution models for the 21 May Concepción earthquake agree with one another in terms of the distribution and position of the main slip in this region, as well as the location of the maximum slip and centroid depth position. This indicates a main rupture below the Arauco peninsula. Despite the few data, our preferred Concepción earthquake slip distribution (model C) fits better the tsunami observations and is consistent with the noninfluence of the 21 May earthquake in the deformation of Mocha Island. Also, model C agrees with the observations about rupture pattern and seismic moment proposed by Cifuentes (1989), a 150 km rupture length, approximately 120 km rupture width and a magnitude $M_w \sim 8.1$. The localized slip distribution of this earthquake is well correlated to the damage produced by this event, mainly located south of the Arauco peninsula (Astroza and Lazo, 2010). The coastline zone was mainly uplifted by the earthquake, which contrasts the systematic coastal subsidence caused by the 22 May Valdivia earthquake that ruptured toward south of the Concepción earthquake (PS70).

The along-dip position of our preferred slip distribution is similar to those of other magnitude $M_w \sim 8.0$ events that have occurred along the Chilean subduction zone. The 21 May Concepción earthquake corresponds to a type C event in the

Lay *et al.* (2012) subduction earthquake classification, similar to the 1975 M_w 7.7 Arauco, 1985 M_w 8.0 Valparaíso (Barrientos, 1988; Bravo *et al.*, 2019), 1995 M_w 8.0 Antofagasta (Ruegg *et al.*, 1996; Pritchard *et al.*, 2002), 2007 M_w 7.7 Tocopilla (Peyrat *et al.*, 2010; Schurr *et al.*, 2012), 2016 M_w 7.6 Chiloé (Lange *et al.*, 2017; Ruiz *et al.*, 2017) earthquakes, and others (Ruiz and Madariaga, 2018). Also, the position of the large asperity of the Concepción earthquake is deeper than the main rupture propagated for the Valdivia megathrust earthquake that was extended from domain B–C to the trench, producing mainly subsidence in the coastline, and therefore a Trans-Pacific tsunami. Along-dip fault segmentation inferred from these deep interplate earthquakes have been associated with different physical controls on the seismogenic interface, such as geometric complexity, sediment loading distribution in the fore-arc, and fault zone rheology. Although some authors describe a possible connection between deeper earthquakes and giant earthquakes at the plate interface (Moreno *et al.*, 2018; Ruiz and Madariaga, 2018), the relationship between the M_w 8.1 Concepción earthquake and M_w 9.5 Valdivia megathrust earthquake is not yet clear and deserves further analyses.

Earthquakes that occurred in domain C of the subduction zone are inefficient generators of tsunamis because they favor uplift of the land rather than beneath the sea (Fig. 3), especially in Chile, where the trench-to-coast distance is smaller than elsewhere (Carvajal and Gubler, 2016). In contrast, earthquake produced by ruptures extending to shallower depths is capable of producing much larger tsunamis, because most of the deformation occurs beneath the sea (Carvajal and Gubler, 2016; Cisternas, Carvajal, *et al.*, 2017). A recent example is the 2015 M_w 8.3 Illapel earthquake, which produced up to 13 m runups (Contreras-López *et al.*, 2016; Fuentes *et al.*, 2016) despite its similar magnitude to the 21 May Concepción earthquake. The few available mareograms from 21 May show instrumental tsunamis with amplitudes typically less than 10 cm, and up to 50 cm in the Talcahuano station, which is the closest to the source region and known for amplifying tsunamis (Farreras, 1978).

The forgotten M_w 8.1 precursor of the M_w 9.5 megathrust earthquake

The M_w 9.5 Valdivia megathrust earthquake slip distribution has been studied by several previously published works (Barrientos and Ward, 1990; Moreno *et al.*, 2009; Fujii and Satake, 2013; Ho *et al.*, 2019), which mainly perform inversions with the PS70 vertical displacement data. Most of them consider the displacement due to the 21 May 1960 Concepción earthquake ascribed by PS70 in their models. Although the 21 May vertical displacements should not influence the main features of their models due to the huge difference in seismic moment, the models of the 22 May 1960 earthquake strictly correspond to the deformation associated with the entire earthquake sequence. This includes from the M_w 8.1 Concepción earthquake on 21 May 1960 to the last large aftershock (M_w 7.7) on 6 June 1960 (Kanamori and Rivera, 2017). Most probably it is also affected by preseismic and eight years of postseismic deformation as observed in recent instrumented great events (e.g., Wang *et al.*, 2018).

Most likely due to the attention raised by the 22 May megathrust earthquake, the 1960 21 May earthquake has not been studied or even mentioned in different modern works on the seismicity of the central-south Chile subduction zone (Ruiz and Madariaga, 2018). Our work confirms the importance of the 21 May earthquake in the context of the large historical Chilean earthquakes and their consideration for earthquake recurrence and seismic hazard analysis in central-south Chile.

Conclusions

Despite the clear limitations of our models due to the few data available, performing a Bayesian inversion and using the land-level changes reported by PS70, we obtained the first slip distribution model for the 21 May 1960 Concepción earthquake. Our model indicates a deep rupture below Arauco peninsula that explains well the mainly uplifted zone ascribed by PS70 and their inefficient tsunami generation. In contrast of the superficial subsidence observations that mainly correspond to offshore slip, as produced by the giant Valdivia megathrust earthquake.

We propose that the Concepción earthquake correspond to an elliptical-shaped rupture 150 km long and 120 km wide, with a total seismic moment of 1.46×10^{21} N · m, equivalent to a moment magnitude M_w 8.1. This earthquake had features similar to those of other $M_w \sim 8.0$ earthquakes that have occurred along the Chilean subduction zone, in which most slip is located in the deepest part of the plate interface, between 20 and 50 km depth, close to the brittle–ductile transition. The small tsunamis recorded along the Chilean coast support such a deep rupture for the 21 May earthquake, in contrast to great Chilean earthquakes that rupture the seismogenic zone, such as the 22 May M_w 9.5 Valdivia megathrust earthquake, which broke the entire plate interface immediately south than the 21 May M_w 8.1 Concepción earthquake.

Data and Resources

The vertical displacement data used in this article (Table S1) come from a published source listed in the references (Plafker and Savage, 1970). Location of earthquakes in Figure 1 is listed in International Seismological Centre (ISC). Mareograms used were first published by Barros and Sievers (1961). Some figures were made using the Generic Mapping Tools (GMT) software version 5.3.1 (Wessel *et al.*, 2013).

Acknowledgments

This work was supported by the Comisión Nacional de Investigación Científica y Tecnológica/Fondo Nacional de Desarrollo Científico y Tecnológico (CONICYT/FONDECYT) Project Number 1170430 and the Programa de Riesgo Sísmico (Actividades de Interés Nacional [AIN], Universidad de Chile). S. R. thanks the support of CONICYT Programa de Investigación Asociativa (PIA)/Anillo de Investigación en Ciencia y Tecnología ACT172002 project "The

interplay between subduction processes and natural disasters in Chile." M. C. acknowledges the support of the Iniciativa Científica Milenio (ICM) through Grant Number NC160025, FONDECYT Project Number 1190258, and the Doctoral program of Geological Sciences of the Universidad de Concepción. The authors also thank the source of the General Bathymetric Chart of the Oceans bathymetry (GEBCO) Grid for their free available bathymetry data, to the Chilean Navy Hydrographic and Oceanographic Service (SHOA) for providing the Nautical charts of Valparaíso, Coquimbo, and Talcahuano, and Alejandra Gubler for her support in the elaboration process of the numerical grids for the tsunami modeling. Finally, the authors are grateful to Associate Editor Allison Bent, as well as three anonymous reviewers for helping improve the manuscript through their constructive comments and suggestions.

References

Altamimi, Z., X. Collilieux, J. Legrand, B. Garayt, and C. Boucher (2007). ITRF2005: A new release of the international terrestrial reference frame based on time series of station positions and earth orientation parameters, *J. Geophys. Res.* **112,** no. B09401, doi: 10.1029/2007JB004949.

Alvarez, L. (1963). Studies made between arauco and Valdivia with respect to the earthquakes of 21 and 22 May 1960, *Bull. Seismol. Soc. Am.* **53,** no. 6, 1315–1330.

Astroza, M., and R. Lazo (2010). Estudio de los daños de los terremotos del 21 y 22 de mayo de 1960, *Proceedings, X Jornadas de Sismología e Ingeniería Antisismica*, Valdivia-Santiago, Chile, 22–27 May 2010 (in Spanish).

Barrientos, S. E. (1988). Slip distribution of the 1985 central Chile earthquake, *Tectonophysics* **145,** nos. 3/4, 225–241.

Barrientos, S. E., and S. N. Ward (1990). The 1960 Chile earthquake: Inversion for slip distribution from surface deformation, *Geophys. J. Int.* **103,** no. 3, 589–598.

Barros, G., and H. Sievers (1961). *El maremoto del 22 de mayo de 1960 en las costas de chile*, Dep. de Navegación e Hidrografía, Valparaíso, Chile, no. 3012, 115 pp. (in Spanish).

Berninghausen, W. H. (1962). Tsunamis reported from the west coast of South America 1562–1960, *Bull. Seismol. Soc. Am.* **52,** no. 4, 915–921.

Bravo, F., P. Koch, S. Riquelme, M. Fuentes, and J. Campos (2019). Slip distribution of the 1985 Valparaíso earthquake constrained with seismic and deformation data, *Seismol. Res. Lett.* **90,** no. 5, 1792–1800, doi: 10.1785/0220180396.

Carvajal, M., and A. Gubler (2016). The effects on tsunami hazard assessment in Chile of assuming earthquake scenarios with spatially uniform slip, *Pure Appl. Geophys.* **173,** 3693–3702, doi: 10.1007/s00024-016-1332-x.

Cifuentes, I. L. (1989). The 1960 Chilean earthquakes, *J. Geophys. Res.* **94,** no. B1, 665–680.

Cifuentes, I. L., and P. G. Silver (1989). Low-frequency source characteristics of the great 1960 Chilean earthquake, *J. Geophys. Res.* **94,** no. B1, 643–663.

Cisternas, M., B. F. Atwater, F. Torrejón, Y. Sawai, G. Machuca, M. Lagos, A. Eipert, C. Youlton, I. Salgado, T. Kamataki, *et al.* (2005). Predecessors of the giant 1960 Chile earthquake, *Nature* **437,** no. 7057, 404–407, doi: 10.1038/nature03943.

Cisternas, M., M. Carvajal, R. Wesson, L. Ely, and N. Gorigoitia (2017). Exploring the historical earthquakes preceding the giant 1960 Chile earthquake in a time-dependent seismogenic zone exploring the historical earthquakes preceding the giant 1960 Chile earthquake, *Bull. Seismol. Soc. Am.* **107,** no. 6, 2664–2675.

Cisternas, M., E. Garrett, R. Wesson, T. Dura, and L. Ely (2017). Unusual geologic evidence of coeval seismic shaking and tsunamis shows variability in earthquake size and recurrence in the area of the giant 1960 Chile earthquake, *Mar. Geol.* **385,** 101–113.

Contreras-López, M., P. Winckler, I. Sepúlveda, A. Andaur-Álvarez, F. Cortés-Molina, C. J. Guerrero, C. E. Mizobe, F. Igualt, W. Breuer, J. F. Beyá, *et al.* (2016). Field survey of the 2015 Chile tsunami with emphasis on coastal wetland and conservation areas, *Pure Appl. Geophys.* **173,** no. 2, 349–367, doi: 10.1007/s00024-015-1235-2.

Cortés, P., P. A. Catalán, R. Aránguiz, and G. Bellotti (2017). Tsunami and shelf resonance on the northern Chile coast, *J. Geophys. Res.* **122,** no. 9, 7364–7379.

Farreras, S. F. (1978). Tsunami resonant conditions of conception bay (Chile), *Mar. Geodes.* **1,** no. 4, 355–360.

Fuentes, M., S. Riquelme, G. Hayes, M. Medina, D. Melgar, G. Vargas, A. Villalobos, *et al.* (2016). A study of the 2015 M_w 8.3 Illapel earthquake and tsunami: Numerical and analytical approaches, *Pure Appl. Geophys.* **173,** no. 6, 1847–1858, doi: 10.1007/s00024-016-1305-0.

Fuis, G. S., P. J. Haeussler, and B. F. Atwater (2015). A tribute to George Plafker, *Quaternary Sci. Rev.* **113,** 3–7.

Fujii, Y., and K. Satake (2013). Slip distribution and seismic moment of the 2010 and 1960 Chilean earthquakes inferred from tsunami waveforms and coastal geodetic data, *Pure Appl. Geophys.* **170,** nos. 9/10, 1493–1509.

Galli, C., and J. Sanchez (1963). Effects of the earthquakes of May 1960 in Concepción and vicinity, *Bull. Seismol. Soc. Am.* **53,** no. 6, 1281–1297.

Ho, T.-C., K. Satake, S. Watada, and Y. Fujii (2019). Source estimate for the 1960 Chile earthquake from joint inversion of geodetic and transoceanic tsunami data, *J. Geophys. Res.* **124,** 2812–2828, doi: 10.1029/2018JB016996.

Kanamori, H., and D. L. Anderson (1975). Amplitude of the Earth's free oscillations and long-period characteristics of the earthquake source, *J. Geophys. Res.* **80,** no. 8, 1075–1078.

Kanamori, H., and J. J. Cipar (1974). Focal process of the great Chilean earthquake May 22, 1960, *Phys. Earth Planet. In.* **9,** no. 2, 128–136.

Kanamori, H., and L. Rivera (2017). An Mw = 7.7 slow earthquake in 1960 near the Aysén fjord region, Chile, *Geophys. J. Int.* **211,** no. 1, 93–106.

Kotani, M., F. Imamura, and N. Shuto (1998). Tsunami run-up simulation and damage estimation using geographical information system, *Proc. Coast. Eng., JSCE* **45,** 356–360.

Lange, D., J. Ruiz, S. Carrasco, and P. Manríquez (2017). The Chiloé Mw 7.6 earthquake of 2016 December 25 in southern Chile and its relation to the Mw 9.5 1960 Valdivia earthquake, *Geophys. J. Int.* **213,** no. 1, 210–221.

Lay, T., H. Kanamori, C. J. Ammon, K. D. Koper, A. R. Hutko, L. Ye, H. Yue, and T. M. Rushing (2012). Depth-varying rupture properties of subduction zone megathrust faults, *J. Geophys. Res.* **117,** no. B04311, doi: 10.1029/2011JB009133.

Linde, A. T., and P. G. Silver (1989). Elevation changes and the great 1960 Chilean earthquake: Support for aseismic slip, *Geophys. Res. Lett.* **16,** no. 11, 1305–1308.

Moreno, M., J. Bolte, J. Klotz, and D. Melnick (2009). Impact of megathrust geometry on inversion of coseismic slip from geodetic data:

Application to the 1960 Chile earthquake, *Geophys. Res. Lett.* **36,** L16310, doi: 10.1029/2009GL039276.

Moreno, M., S. Li, D. Melnick, J. R. Bedford, J. C. Baez, M. Motagh, S. Metzger, S. Vajedian, C. Sippl, B. D. Gutknecht, *et al.* (2018). Chilean megathrust earthquake recurrence linked to frictional contrast at depth, *Nat. Geosci.* **11,** 285–290, doi: 10.1038/s41561-018-0089-5.

Okada, Y. (1985). Surface deformation due to shear and tensile faults in a half-space, *Bull. Seismol. Soc. Am.* **75,** no. 4, 1135–1154.

Peyrat, S., R. Madariaga, E. Buforn, J. Campos, G. Asch, and J. Vilotte (2010). Kinematic rupture process of the 2007 Tocopilla earthquake and its main aftershocks from teleseismic and strong-motion data, *Geophys. J. Int.* **182,** no. 3, 1411–1430.

Plafker, G. (1972). Alaskan earthquake of 1964 and Chilean earthquake of 1960: Implications for arc tectonics, *J. Geophys. Res.* **77,** no. 5, 901–925.

Plafker, G., and J. Savage (1970). Mechanism of the Chilean earthquakes of May 21 and 22, 1960, *Geol. Soc. Am. Bull.* **81,** no. 4, 1001–1030.

Pritchard, M., M. Simons, P. Rosen, S. Hensley, and F. Webb (2002). Co-seismic slip from the 1995 July 30 Mw = 8.1 Antofagasta, Chile, earthquake as constrained by InSAR and GPS observations, *Geophys. J. Int.* **150,** no. 2, 362–376.

Radiguet, M., F. Cotton, M. Vergnolle, M. Campillo, B. Valette, V. Kostoglodov, and N. Cotte (2011). Spatial and temporal evolution of a long term slow slip event: The 2006 Guerrero slow slip event, *Geophys. J. Int.* **184,** no. 2, 816–828.

Ruegg, J. C., J. Campos, R. Armijo, S. Barrientos, P. Briole, R. Thiele, M. Arancibia, J. Cañuta, T. Duquesnoy, M. Chang, *et al.* (1996). The Mw = 8.1 Antofagasta (north Chile) earthquake of July 30, 1995: First results from teleseismic and geodetic data, *Geophys. Res. Lett.* **23,** no. 9, 917–920, doi: 10.1029/96GL01026.

Ruiz, S., and R. Madariaga (2018). Historical and recent large megathrust earthquakes in Chile, *Tectonophysics* **733,** 37–56.

Ruiz, S., E. Klein, F. del Campo, E. Rivera, P. Poli, M. Metois, C. Vigny, J. C. Baez, G. Vargas, F. Leyton, *et al.* (2016). The seismic sequence of the 16 September 2015 Mw 8.3 Illapel, Chile, earthquake, *Seismol. Res. Lett.* **87,** no. 4, 789–799, doi: 10.1785/0220150281.

Ruiz, S., M. Moreno, D. Melnick, F. Del Campo, P. Poli, J. C. Baez, F. Leyton, and R. Madariaga (2017). Reawakening of large earthquakes in south central Chile: The 2016 Mw 7.6 Chiloé event, *Geophys. Res. Lett.* **44,** no. 13, 6633–6640, doi: 10.1002/2017GL074133.

Saint-Amand, P. (1961). Los terremotos de mayo-Chile 1960: An eyewitness account of the greatest natural catastrophe in recent history, *Technical Article 14*, U.S. Naval Ordinance Test Station, China Lake, California, 39 pp.

Schurr, B., G. Asch, M. Rosenau, R. Wang, O. Oncken, S. Barrientos, P. Salazar, and J.-P. Vilotte (2012). The 2007 M7.7 Tocopilla northern Chile earthquake sequence: Implications for along-strike and down-dip rupture segmentation and megathrust frictional behavior, *J. Geophys. Res.* **117,** no. B05305, doi: 10.1029/2011JB009030.

Sievers, H., G. Villegas, and G. Barros (1963). The seismic sea wave of 22 May 1960 along the Chilean coast, *Bull. Seismol. Soc. Am.* **53,** no. 6, 1125–1190.

Tarantola, A. (2005). *Inverse Problem Theory and Methods for Model Parameter Estimation*, SIAM, Philadelphia, Pennsylvania.

Tassara, A., and A. Echaurren (2012). Anatomy of the Andean subduction zone: Three dimensional density model upgraded and compared against global-scale models, *Geophys. J. Int.* **189,** no. 1, 161–168.

Thomas, H., W. Bowes, and S. N. Bravo (1963). Field observations made between Puerto Montt and Maullín, *Bull. Seismol. Soc. Am.* **53,** no. 6, 1353–1356.

Wang, K., T. Sun, L. Brown, R. Hino, F. Tomita, M. Kido, T. Fujiwara, *et al.* (2018). Learning from crustal deformation associated with the M9 2011 Tohoku–Oki earthquake, *Geosphere* **14,** no. 2, 552–571.

Wang, X. (2009). *User Manual for COMCOT Version 1.7 (First Draft)*, Cornel University, New York, New York, 65 pp.

Weischet, W. (1963). Further observations of geologic and geomorphic changes resulting from the catastrophic earthquake of May 1960, in Chile, *Bull. Seismol. Soc. Am.* **53,** no. 6, 1237–1257.

Wessel, P., W. H. Smith, R. Scharroo, J. Luis, and F. Wobbe (2013). Generic mapping tools: Improved version released, *Eos Trans. AGU* **94,** no. 45, 409–410.

Manuscript received 17 June 2019
Published online 11 March 2020